

Exploration of Terahertz Imaging with Silicon MOSFETs

Alvydas Lisauskas · Maris Bauer · Sebastian Boppel · Martin Mundt · Bassam Khamaisi · Eran Socher · Rimvydas Venckevičius · Linas Minkevičius · Irmantas Kašalynas · Dalius Seliuta · Gintaras Valušis · Viktor Krozer · Hartmut G. Roskos

Received: 10 May 2013 / Accepted: 18 December 2013 /

Published online: 9 January 2014

© Springer Science+Business Media New York 2014

Abstract We summarize three lines of development and investigation of foundry-processed patch-antenna-coupled Si MOSFETs as detectors of THz radiation: (i) Exploiting the principle of plasma-waved-based mixing in the two-dimensional electron gas of the transistors' channels, we demonstrate efficient detection at frequencies as high as 9 THz, much above the transit-time-limited cut-off frequencies of the devices (tens of GHz). Real-time imaging at 600 GHz with a 12×12 detector array is explored. (ii) Given the limited THz power usually available for applications, we explore imaging with enhanced sensitivity in heterodyne mode. We show that real-time operation of a 100×100 -pixel heterodyne camera should be possible at 600 GHz with a better dynamic range (30 dB) than for direct power detection (20 dB), even if only a quarter-milliwatt of local-oscillator power, distributed radiatively over all detector pixels, is available. (iii) Finally, we present an all-electronic raster-scan imaging system for 220 GHz entirely based on CMOS devices, combining the CMOS detectors with an emitter circuit implemented in a 90-nm CMOS process

A. Lisauskas (✉) · M. Bauer · S. Boppel · M. Mundt · V. Krozer · H. G. Roskos (✉)
Physikalisches Institut, Johann Wolfgang Goethe-Universität Frankfurt,
D-60438 Frankfurt am Main, Germany
e-mail: alvydas.lisauskas@ff.vu.lt
e-mail: roskos@physik.uni-frankfurt.de

A. Lisauskas
Faculty of Physics, Vilnius University, LT-10222 Vilnius, Lithuania

B. Khamaisi · E. Socher
School of Electrical Engineering, Tel Aviv University, IL-6978 Tel Aviv, Israel

R. Venckevičius · L. Minkevičius · I. Kašalynas · D. Seliuta · G. Valušis
Semiconductor Physics Institute, Center for Physical Science and Technology,
LT-01108 Vilnius, Lithuania

and delivering radiation with a power on the 100- μ W scale. Considering progress in the field, we anticipate that the emitter concept of oscillator-based power generation with on-chip frequency multiplication will carry well into the sub-millimeter-wave regime.

Keywords Terahertz emitters and detectors · Silicon CMOS circuits · Heterodyne detection · Terahertz imaging

1 Introduction

Imaging and sensing in the terahertz (THz) frequency range of electromagnetic radiation has made considerable progress in recent years. This frequency regime has proven to be of importance for a plethora of applications, both in science and beyond, such as security and safety screening, process monitoring and non-destructive material testing, biological, medical and pharmaceutical analysis, communications, etc. [1–9]. However, up to now, most THz applications are restricted to dedicated, bulky and generally immobile laboratory-type setups while compact, transportable sensors are lacking. This situation might change soon owing to recent advances in the research on THz systems based on integrated microelectronics. Circuit-based emitters conquer the regime of hundreds of GHz and begin to reach up to 1 THz [10–13], and detection based on internal mixing in field-effect transistors has experienced enormous progress, some of which will be described in this paper. With a view towards future low-cost practical applications, it is highly promising that emitters and detectors can be fabricated in reproducible, high-yield processes using foundry-level complementary metal-oxide semiconductor (CMOS) technology [14, 15].

Especially THz detectors have enjoyed enormous progress in recent years, with the consequence that the first all-CMOS focal-plane arrays and full cameras with field-effect transistors (FETs) as detector elements have been demonstrated in 2012 in real-time-imaging mode in the sub-1-THz frequency regime [16, 17]. This development is supplemented by parallel advances concerning CMOS Schottky-diode detector arrays [18]. Microbolometer detector arrays, reaching down from the infrared spectral regime, have conquered the THz realm down to 1.5 THz [19, 20]. The detectors are built directly on CMOS read-out chips with some additional processing steps for the actual sensors. There is hence good reason to state that silicon CMOS technology has taken a strong foothold in THz photonics and is in the process of converting it rapidly into a technology much better atuned to market requirements than it was before.

This paper puts the focus on THz MOSFET detectors—which we term TeraFET detectors in the following—and arrays thereof, and summarizes the three lines of research outlined in the abstract. It begins with an exploration of possible high-frequency limits of the detection principle, considers the heterodyne and sub-harmonic detection modalities, and finally describes the first steps towards an all-CMOS measurement system.

2 Direct Detection

Detection Principle In 1996, Dyakonov and Shur proposed the application of FETs for the detection of high-frequency signals especially in the THz range [21]. Based on a hydrodynamic transport model, they considered the charge-carrier dynamics in the FET's two-dimensional electron gas under the influence of a GHz or THz gate-voltage modulation, and predicted rectification to occur in conjunction with the excitation of charge density oscillations. Later, it was shown, that this plasmonic type of rectification is an extension of rectification by resistive mixing, a well-known process in the quasi-static limit of FET operation [22], which is sometimes also termed square-law detection because the rectified signal depends on gate voltage quadratically (the drain current being determined by the gate voltage times the channel conductance which also depends on gate voltage) [23, 24]. With increasing frequency, plasma waves appear in the channel and influence the rectification process. First they are overdamped, before they fully develop when the frequency becomes larger than the plasma damping rate. For MOSFETs at room temperature, this happens at frequencies above 1 THz [15, 25]. If the boundary conditions are chosen correctly [25, 26], rectification can occur in all regimes, in the transition regime (where it is known as non-resonant detection [21, 27], respectively distributive resistive mixing [22, 23]) as well as in the full-plasmonic regime. Interestingly, the responsivity should increase by a factor of three as the transition regime is crossed [21, 25], although this prediction has not been verified experimentally yet because the responsivity (in units of V/W or A/W) rolls off at THz frequencies as a consequence of parasitic capacitance and resistance effects (see below). If the channel is short enough, standing plasma waves and sensitivity enhancement at the resonance frequencies are predicted for the full-plasmonic regime [21], but until now, these have not been observed in the case of MOSFETs, only for III-V high-electron-mobility transistors at low temperature [28, 29].

The most important figure of merit for this kind of detector is the noise-equivalent power (NEP). Since THz detection with silicon MOSFETs was first observed [30], the NEP of the detectors has been improved continuously and now is in the range of a few tens of $\text{pW}/\sqrt{\text{Hz}}$ for state-of-the-art devices at room temperature [25, 31–33]; it reaches down to $\geq 1 \text{ pW}/\sqrt{\text{Hz}}$ at cryogenic temperatures [15]. Performance hence is similar to that of Schottky detectors. While the responsivity can be enhanced significantly by a drain current bias, when the pinch-off conditions are approached and reached [34–37], the noise increases concomitantly and the signal-to-noise ratio is predicted to improve marginally at best, but in experiments, rather a performance decrease has been observed until now [38].

A successful way to enhance sensitivity of TeraFET detectors is heterodyne operation by mixing of the (weak) signal to be detected with an intensive signal in the device [39, 40]. The intensive signal is usually termed local-oscillator signal, although it may be provided radiatively to the detector(s) in the same way as the weak signal to be measured. Detection at difference frequencies in the MHz or even GHz regime, where the noise is lower than in the kHz range, is possible because the response of the TeraFETs is comparably fast like that of Schottky diodes, and much

faster than that of thermal detectors such as bolometers. Heterodyne mixing is usually employed to boost the sensitivity only of individual detectors, because it requires a considerable amount (up to 1 mW) of local-oscillator power to reach best mixing performance. We report later, however, about experiments which show that also multi-pixel detection can benefit and exhibit an improved signal-to-noise ratio even if the available local oscillator power is distributed over the detector array providing only power on the sub- μ W level per pixel. Because power availability becomes more and more limited with rising THz frequency, heterodyne detection loses its appeal at high sub-THz frequencies. As an alternative, we currently explore subharmonic mixing, where the local-oscillator frequency is a fraction (plus a frequency offset) of the signal frequency, and remains in a frequency range where power is still readily available. This promising approach is not discussed further in this paper, we refer the interested reader to Refs. [41, 42].

Detector Implementation This section describes the implementation of TeraFET detectors, which are later applied to imaging and spectroscopy. These detectors are fabricated in commercially available CMOS technology with transistors acting as rectifying elements. Generally, TeraFET detection benefits from the scaling trends of semiconductor technology and the reduction of technology's parasitic effects. Even though detection sensitivity is not transit-time limited and thus is not influenced by the channel length, the Johnson-Nyquist noise dominant in TeraFET detection, can be effectively reduced with smaller node-size technologies. Also the parasitic effects, which mainly cause performance roll-off at THz frequencies, are better controlled with newer technologies.

Besides the intrinsic property of the nonlinear element to rectify, when implementing a detector it is very important to optimize power transfer i.e., to ensure good power matching and reduced power loss. Moreover, even when the power transfer is good, higher sensitivity will have the detector with higher channel impedance. Therefore, for TeraFETs the use of high impedance antennas (which are considerably narrow-band) is preferable. In this case the detection bandwidth is mainly determined by antenna properties and not by FET. Additionally, the standard CMOS processes usually use lossy silicon substrates complicating broad-band antenna designs. However, with increasing frequency in the terahertz range electromagnetic fields are contained in smaller volume resulting in the increase of antenna design freedom.

This paper describes devices from two generations of optimization. In both generations, we decided to work with monolithically integrated patch antennas, as they have a relatively high antenna impedance and naturally shield radiation from the lossy substrate. The frequency-response bandwidth is determined by the patch antenna with a full width at half maximum of about 8–10 % of the center frequency.

The first-generation TeraFETs were designed for ten different resonance frequencies spanning from 213 GHz to 4.08 THz and were implemented on a 1.5 mm \times 2.5 mm large silicon die using the 150-nm CMOS process provided by LFoundry GmbH. A pair of transistors acts as rectifying elements for which low-leakage transistors with a 150-nm channel length and a 320-nm gate width were selected. The transistor cutoff frequency is approximately 35 GHz at threshold and approximately 65 GHz in the strong-inversion regime, thus the detectors will be operated far above

their cut-off frequencies. It is important to note, that device cut-off frequencies although do not limit the rectification efficiency, they set the limit to the intrinsic modulation bandwidth. In this generation of designs, pairs of transistors instead of individual ones were chosen in order to have a well-defined virtual a.c. ground in the center of symmetry of the device, at the penalty of halving the rectified signal.

Figure 1 illustrates the basic design of a 595-GHz detector. The radiation (with its polarization vector in the paper plane) is received by a patch antenna, which is integrated into the metal / insulator stack of the CMOS process. A patch antenna commonly consists of two metal sheets—a ground plane and a metal patch—and the dielectric in-between. For the ground plane, the first metal layer—the one closest to the substrate—is used. At 595 GHz, the topmost metal layer is employed for the patch. Its geometric size of $109\ \mu\text{m} \times 118\ \mu\text{m}$ is three orders of magnitude larger than the transistor size. The geometric dimensions of the patch scales approximately quadratically with wavelength. At larger frequencies, intermediate metal layers are chosen for the patch, thus moving the antenna into the dielectric, in order to keep antenna performance high. This also reduces the *optical height* between patch and ground plane from $12.8\ \mu\text{m}$ to lower values, where *optical height* is defined as the product of the geometric height and the refractive index. The layout parameters are summarized in Table 1. From both edges of the patch, THz signals are guided downwards vertically to the two MOSFETs, which correspondingly are fed with signals of opposing signs. The feeds are realized as vias. The transistors rectify the signals, with each transistor generating a d.c. sourcedrain voltage, which is ready for read-out through the antenna patch.

A second generation of detectors was implemented based on an analytic device model, which is an extension of the intrinsic analytical model derived in Ref. [25] by parasitic effects mainly determined by the junction, overlap and fringe capacitances as well as by series resistances of the MOSFETs. These parasitic contributions

Fig. 1 Basic layout of the MOSFET detectors described in Ref. [25] (first-generation devices). They were fabricated in 150-nm CMOS technology (i.e., with a channel length of 150 nm; the channel width is 320 nm) and consist of a monolithically integrated patch antenna connected to the drain contacts of a pair of transistors working as rectifying elements. A metal layer (M1) above the silicon surface serves as ground plane; the oxo-nitride insulation layers, which add up to a total optical height of $12.8\ \mu\text{m}$, serve as the antenna dielectric. The rectified signal is read out at the antenna center (ac ground)

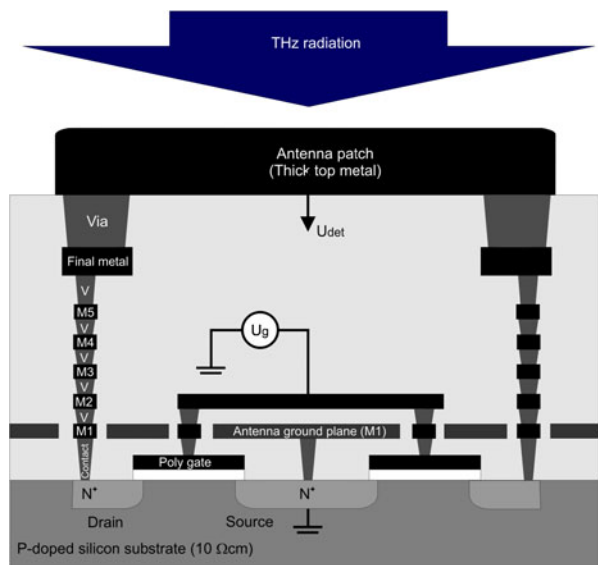


Table 1 Summarizing important layout parameters and measurement results for the TeraFET detectors: The transistor size is defined as number of transistors used times gate length times gate width; The size of the antenna is given as the patch size, which is 3 orders of magnitude larger than the transistor size; The optical height is defined as the product of the geometric distance between ground plane and patch, and the refractive index. By the experimental characterization, the antenna resonance frequency, the responsivity of the TeraFET and its NEP value are evaluated

	Layout parameter			Measured results		
	Transistor size nm ²	Geometric patch size μm ²	Optical height μm	Resonance frequency THz	Respon- sivity V/W	NEP pW/√Hz
☆	2 × 150 × 320	321 × 375	12.8	0.213	37	398 ^b
⬡	2 × 150 × 320	241 × 281	12.8	0.282	62	238 ^b
◯	2 × 150 × 320	218 × 236	12.8	0.320	65	227 ^b
●	2 × 150 × 320	109 × 118	12.8	0.595	351	42 ^b
■	2 × 150 × 320	92 × 100	12.8	0.695 ^a	360 ^a	41 ^b
▲	2 × 150 × 320	45 × 49	4.7	1.44	97	152 ^b
▼	2 × 150 × 320	36 × 40	4.7	1.74	55	268 ^b
◆	2 × 150 × 320	23 × 26	2.9	2.50	12	1229 ^b
◀	2 × 150 × 320	19 × 21	2.9	2.94	30	491 ^b
▶	2 × 150 × 320	15 × 16	1.0	4.075	4.6	3204 ^b
+	1 × 90 × 120	25.5 × 25.5	4.9	2.52 ^a	336 ^a	63
×	1 × 90 × 120	20.3 × 20.3	4.9	3.11 ^a	308 ^a	85
✱	1 × 90 × 120	14.5 × 14.5	4.9	4.25 ^a	230 ^a	110

^aThis value relies on a discrete line of a THz gas laser: Therefore the antenna resonance frequency could not be determined—instead, the frequency of the closest line used is given. The responsivity is determined at this laser line

^bNEP estimate relies on average resistance values

become increasingly important at frequencies deep in the THz region of the spectrum and the plasmonic regime of device operation. With the analytical expressions for detector impedance, detector responsivity and NEP from Ref. [25], embedded in an equivalent-circuit description which includes the parasitic effects, we estimated the performance to be expected for different process technologies. This led to an implementation of TeraFET detectors for 2.54, 3.13 and 4.25 THz in a 90-nm CMOS process provided by United Microelectronics Cooperation (UMC). Transistors with 90-nm channel length and a 120-nm gate width were selected for these frequencies, and for the sake of achieving better responsivity and NEP values, a single-transistor solution was favored over a symmetric layout of the TeraFET detectors. The design optimization process involved—in addition to the reduction of the influence of parasitic circuit elements—the fine-tuning of the patch-antenna for impedance matching.

Direct Detection up to 9 THz In Fig. 2, we present voltage responsivity values for different TeraFET detectors of both generations. For characterizations at and below 600 GHz, we used electronic multiplier-based sources. Five detector pixels above 1 THz were characterized with the free-electron-laser source FELBE at the Helmholtz-Zentrum Dresden-Rossendorf, Dresden, Germany. The pulse length was up to a few 10 ps, depending on the frequency. As both sources are tunable, the resonance behavior of the antennas of the detectors could be determined. Starting from the lower frequency side, the best measured performance of resonant detectors of the first generation are found at 0.695 THz; above this value, the responsivity decreases with increasing frequency. The resonance frequencies of 0.213, 0.282, 0.320, 0.595, 1.44, 1.74, 2.5, 2.94, and 4.08 THz were determined for the first-generation detectors, which are values close to the design frequency. Corresponding optical responsivities of 37, 62, 65, 351, 97, 55, 30, and 4.6 V/W are achieved at the resonances. Moreover, each patch also shows resonances at odd harmonics as displayed for the 2.94-THz pixel which also exhibits a response at 8.4 THz. Detectors at and above 585 GHz were also characterized with continuous-wave radiation from discrete lines of a CO₂-laser-pumped molecular gas laser. These measurements show good agreement with the other measurements considering that different sample pixels were used.

Second-generation detectors implemented in 90-nm technology are represented in Fig. 2 by crosses. These devices do not show the previously measured strong roll-off at high frequencies, an improvement which can be mainly attributed to antenna

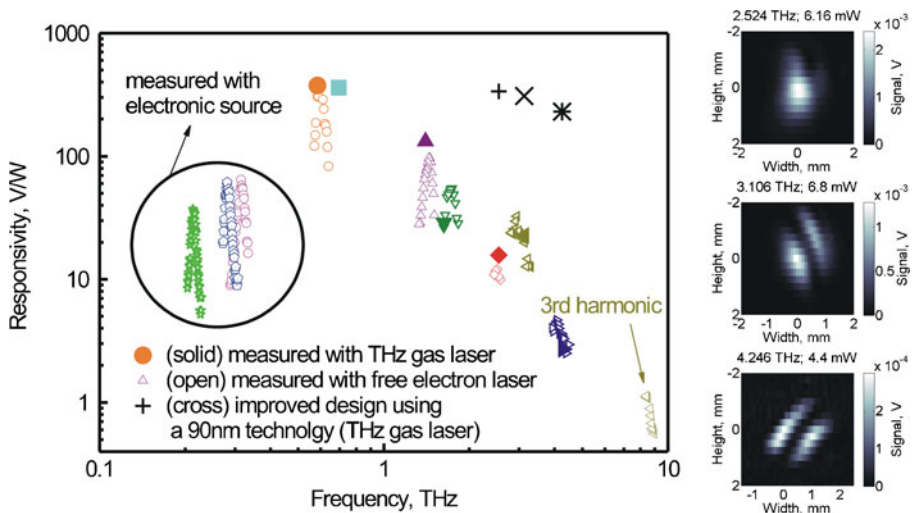


Fig. 2 Left side: Responsivity of the two generations of TeraFETs fabricated using a 150-nm and 90-nm technology. The devices, specified in Table 1 and marked by the symbols defined there, were characterized using three different radiation sources. 150-nm-type devices: discrete lines of a CO₂-pumped molecular gas laser (solid symbols), tunable pulsed radiation of a free-electron laser (open symbols at high frequencies), and electronic sources based on multiplier chains (open symbols at low frequencies). Crosses show the latest results for optimized structures implemented in a 90-nm technology, characterized with the molecular gas laser. Right side: Beam profiles of the gas laser at various frequencies, measured with the second-generation TeraFET detectors via raster scanning

design, reduction of parasitic effects and impedance matching. The responsivity values of 336, 308, and 230 V/W were measured for frequencies of 2.52, 3.11 and 4.25 THz, respectively.

For all three different types of sources, TeraFET samples were characterized by a THz beam for which the total beam power was previously determined by a calibrated power meters. To determine responsivity, the beam spot was always scanned by the TeraFET detector. As an example, the right side of Fig. 2 displays beam profiles measured with the second-generation TeraFET detectors at 2.52, 3.11, 4.25 THz. The beam profiles reveal that the THz gas laser operates at higher-order cavity modes besides the first-order mode. The spectroscopic measurements, which are discussed in the next section were performed using these beams.

Raster-scan Spectroscopic Imaging As described above, the THz FET detectors fabricated in the 90-nm CMOS process have been designed for various selected frequencies in correspondence to the emission lines of a CO₂-pumped molecular gas laser. With this source-detector combination, spectroscopic THz imaging is demonstrated.

The experimental setup is shown in Fig. 3. The continuous-wave THz beam is modulated at a frequency of around 1 kHz by a mechanical chopper and split into the main and reference beams. The reflected part of the beam is focused on a reference detector, which is used for monitoring the laser output power. The transmitted beam is guided to the sample—placed at an intermediate focus—by a 4-inch off-axis parabolic (OAP) mirror. The radiation, which is transmitted through the sample is collimated and focused by a set of 4-inch and 2-inch OAPs onto the CMOS detector chip, which consists of a linear array of closely spaced, patch-antenna-coupled MOSFETs. Since the laser emits radiation at single frequencies and gases have to be changed to switch laser lines, images were recorded only for a single frequency at a time. However, with a suitable broadband THz source, multispectral imaging could be performed in parallel by simultaneous detector read-out. Finally, the rectified THz signal is recorded by a lock-in amplifier with an integration time constant of 10 ms.

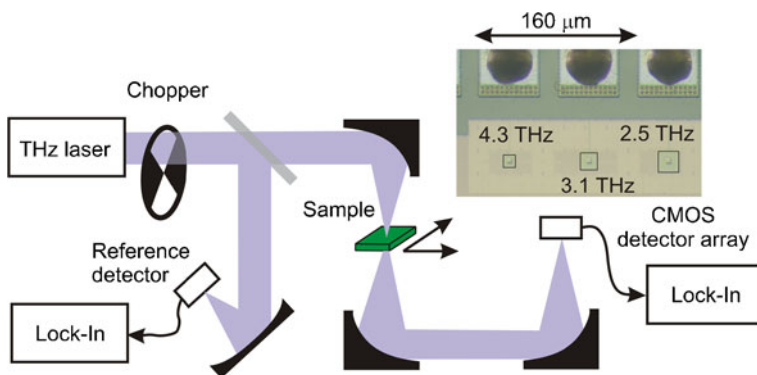


Fig. 3 Experimental set-up for raster-scan spectroscopic transmission mode imaging

For the spectroscopic imaging, explosive simulants with characteristic absorption lines in the THz spectral range were chosen, i.e., sucrose (SC) as a simulant for penthrite (PETN) and tartaric acid (TA) as a simulant for hexogen (RDX) [43, 44]. The components were mixed with Teflon (PTFE) powder and were pressure-formed into thin pellets of 13 mm diameter and a thickness of 1.3 mm. Three samples were manufactured, containing 10 % SC, 10 % TA and a mixture of 5 % SC and 5 % TA, respectively. A fourth sample—a pure PTFE pellet—was prepared as a reference material.

In Fig. 4a, the measured THz transmission image is shown for a 3.1 THz frequency. Without changing the positions of samples we have raster-scanned the pellets at five discrete frequencies: 0.76, 1.8, 2.52, 3.11 and 4.25 THz. The procedure, however requested once changing the gas in the laser cavity and for each frequency point to realign detectors both accordingly to the polarization of emitted radiation and the location of focus. Figure 4b presents the comparison of the resulting average transmission values with the continuous spectra recorded using Fourier-Transform Infrared spectrometer equipped with Golay cell detector. Since the data recorded with TeraFET detectors correspond well with the reference detector, from these measurements we can indirectly conclude that detectors were responding linearly to the power. In our earlier experiments, attenuating with paper sheets, the linearity range for similar TeraFETs was found to be not worse as 35 dB at 600 GHz.

We are able to conclude that for presented THz frequencies, measured the pellets are clearly distinguishable. It is interesting to note, that visible inhomogeneities within the pellet area are believed to be less related to signal noise, but rather show granulation of the simulants, possibly introduced during fabrication of the samples.

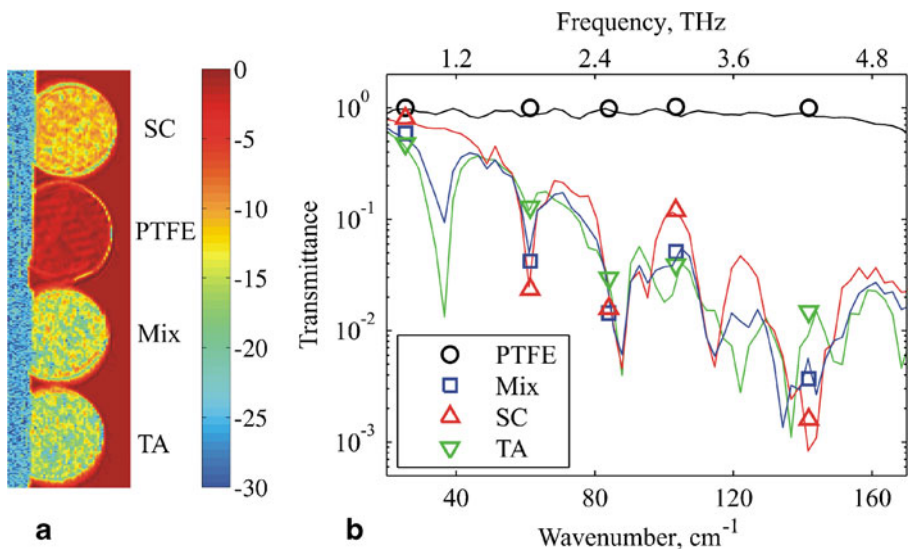


Fig. 4 **a** Transmission images of four pellets at 3.1 THz frequency. The intensity scale is logarithmic. **b** The average transmittance of pellets recorded with CMOS detectors at discrete frequencies (symbols) and measured with Fourier-Transform spectrometer (lines) using a Golay cell detector

Real-time Imaging at 600 GHz with a 12×12 Detector Array In this section we want to report on the realization of a real-time multi-pixel THz camera. Fabrication of an image sensor with a large pixel count requires a reliably high yield in the production process. Standard CMOS technology foundries offer such high yields and at the same time allow the integration of large multi-pixel arrays on one chip instead of having to build arrays of separate detector devices. Thus, the employment of silicon MOSFET detectors in large focal-plane arrays is a very promising approach towards THz cameras. Based on the previously discussed detector technology, a focal plane array of MOSFET detectors has been fabricated in a 150-nm CMOS foundry process. The multi-pixel detector chip, used as the camera's image sensor, consists of four quadrants of 12×12 single pixels, resulting in a total of 576 pixels. For the discussion and results presented in this section, a single quadrant of 12×12 pixels has been read out. The pixel pitch is $195 \mu\text{m}$ in both directions, amounting to an active sensor area of $2.34 \times 2.34 \text{ mm}^2$ for the single quadrant.

At the top of Fig. 5, a magnified optical photograph of the camera's image sensor is shown on the right. Each detector pixel consists of two FETs in a symmetric

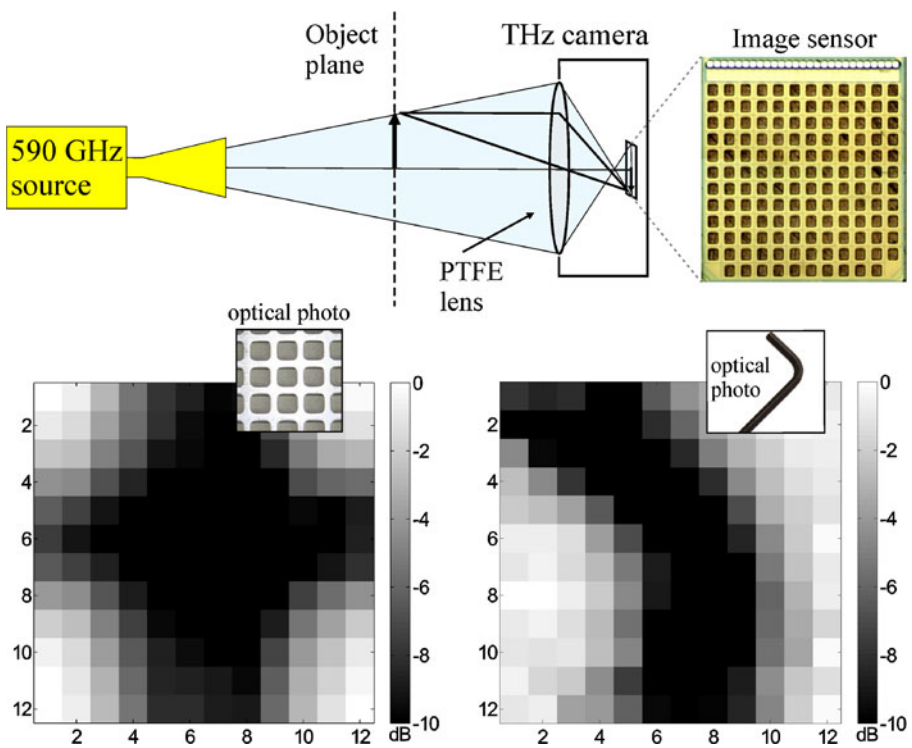


Fig. 5 At the top, the THz camera setup with plane-to-plane imaging geometry is illustrated. The electronic 590 GHz source illuminates the object plane, which is imaged onto the image sensor, implemented as a 12×12 MOSFET focal plane array (magnified optical photograph shown). At the bottom, two THz transmission images (Left: metal grating, Right: upper part of a hex key) acquired in continuous camera operation mode are displayed

arrangement (circuitry previously shown in [17]), with the transistor's drain contacts differentially coupled to a common top-layer patch antenna. Read-out is realized via the antennas virtual ac ground, i.e. the axis of symmetry of the patch. The metal patches have been optimized for a resonance frequency of 590 GHz with a detection bandwidth of the antennas of about 10 % of this center frequency.

During camera operation, the sensor rows are read-out successively by the help of additionally implemented FET switches, enabling selected application of the gate bias voltage to the active line of pixels. For each row read-out sequence, all 12 sensor columns are processed in parallel in about 2.5 ms. By this procedure, a full-frame acquisition rate of 33 Hz could theoretically be achieved. However, the present stage of development of data processing algorithms limits the effective frame-rate to 16 frames-per-second (fps), already providing real-time operation of the image sensor.

In order to determine the single-detector responsivity and noise-equivalent power (NEP), a beam profile of an all-electronic 590 GHz source has been acquired in continuous camera operation mode in a 2f-2f geometry. The averaged single-pixel voltage responsivity \mathfrak{R}_V can be calculated via the sum of the voltage responses R_V of all pixels, divided by the total available power in the illuminating beam [16]

$$\mathfrak{R}_V = \frac{\frac{\pi}{\sqrt{2}} \sum_{ij} R_V^{ij}}{P_{\text{tot}}} \quad (1)$$

The numerical prefactor takes into account the rms value of the square-wave-modulated source signal as detected by the digital lock-in read-out. With an available beam power of 260 μW , a responsivity of 348 V/W could be determined from the recorded beam profile. From this number, the single-pixel NEP can be calculated as the ratio of the rms noise voltage R_{noise} of the detector—determined as the average detector voltage response with blocked signal—and the detector responsivity:

$$\text{NEP} = \frac{R_{\text{noise}}}{\mathfrak{R}_V} \quad (2)$$

For our camera, in continuous operation mode at 16 fps, we find a minimum resolvable power $\text{NE}\Delta P$ (we introduce this figure-of-merit in order to differentiate the camera-operation mode from the single detector NEP) of 15.2 nW. At the current stage of development, this value of the camera sensitivity is mainly dominated by adc noise in the read-out electronic circuit.

Under the mentioned conditions of 2.5 ms acquisition time per line (i.e. a noise bandwidth of $\Delta f = 400\text{Hz}$), a theoretical $\text{NE}\Delta P$ of 0.9 nW per frame can be expected, taking into account an averaged single-pixel NEP of 43pW/ $\sqrt{\text{Hz}}$ as determined from lock-in measurements. In order to enhance the image sensor performance, low-noise amplifiers have been included for each line of the camera chip. With this improvement, we already achieved a responsivity of 23.5 kV/W and an $\text{NE}\Delta P$ of 9.6 nW which is still about 10 dB worse than the anticipated value and requires further improvement. Nevertheless, these results compares well with reported $\text{NE}\Delta P$ of 12 nW at 25 fps for a 33×33 pixel FET-based camera implemented using 65-nm CMOS technology [16].

Figure 5 illustrates the plane-to-plane imaging setup at the top, showing the implementation of the described multi-pixel MOSFET array as an image sensor in a THz camera. An all-electronic source working at 590 GHz is used to illuminate the object plane. The camera is operated with a single aspherical short-focal-length Teflon (PTFE) lens ($f = 2.5$ mm), which has been optimized for imaging applications. The geometry has been arranged in a way that the object-plane is imaged onto the image sensor with a demagnification factor of 30 %.

At the bottom of Fig. 5, two THz transmission images are shown, which have been recorded as single shots during continuous camera operation mode at 16 fps. The image on the left displays transmission through a metallic grating with square openings of 5 mm edge length and a spacing of 2.5 mm. On the right, the bending of the upper part of a 2 mm hex key can be identified. The dynamic range for both images clearly exceeds 10 dB. The total available beam power distributed over the sensor plane was $260 \mu\text{W}$ and the resulting beam power on the sensor chip area of 5.5 mm^2 was $104 \mu\text{W}$, as has been extracted from a previous calibration measurement without the objects. A video showing real-time operation of the THz camera is presented in supplementary material.

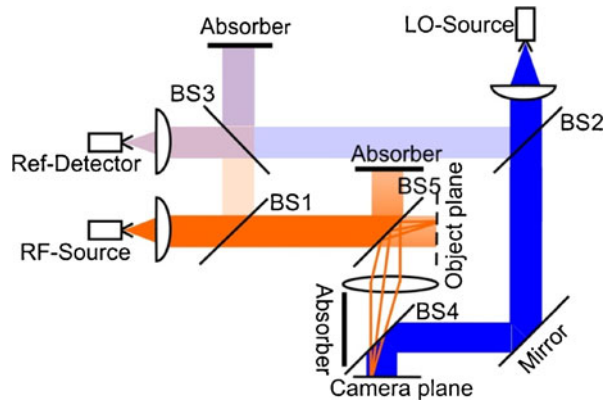
Comparing with other technologies, TeraFET imagers (both presented here and at [16]) do not yet reach performance of microbolometer-based cameras which greatly benefit from optimized infrared manufacturing process and read-out procedures developed for thermal imaging. These devices report device $\text{NE}\Delta\text{P}$ values reaching well down to the levels of few tens of pW and single pixel NEP of the order of few $\text{pW}/\sqrt{\text{Hz}}$ [20, 45, 46]. However, in lower THz frequency range where the performance of microbolometer imagers is much worse, the microbolometer and TeraFET approaches are already competitive.

Future work concerning the performance of the presented camera is dedicated towards two major promising directions. First, as discussed above, improvement of the read-out circuitry is expected to increase the camera sensitivity by a possible factor of ~ 20 . Second, as will be shown in the following section, MOSFET-based THz detectors readily permit operation in heterodyne mode. Hence, improvements of the detector sensitivity as well as the phase-detection capability, allowing for the reconstruction of tomographic object information, can further enhance the imaging quality. Besides the common approach to include another external local oscillator source to illuminate the sensor area, current investigations are focused on the on-chip generation of LO power, with the oscillators to be included in the CMOS circuit design.

3 Imaging in Heterodyne Mode

In order to illustrate the advantages of heterodyne detection, we performed tests at 591.4 GHz at the conditions relevant for camera operation [47]. By scanning a line of several detectors across the image plane, we emulated a focal-plane array of 100×100 pixels with resulting active area of $20 \times 20 \text{ mm}^2$. The experimental setup is presented in Fig. 6. For object illumination, we used a RF source with total output power of $432 \mu\text{W}$. For a lock-in integration time of 20 ms and 6 dB/oct filter (corresponding

Fig. 6 Setup for heterodyne imaging in reflection geometry in plane-to-plane configuration. Image reproduced from [48]



to an effective frame rate of 12.5 Hz), the maximal dynamic range turned out to be 20 dB. This is only sufficient for scenes with large contrast. As the radiation power available for object illumination is usually limited and expensive, it is desirable to enhance the sensitivity of the detectors. One way to achieve this is by a heterodyne approach. It also requires additional radiation power from a local oscillator (LO), and

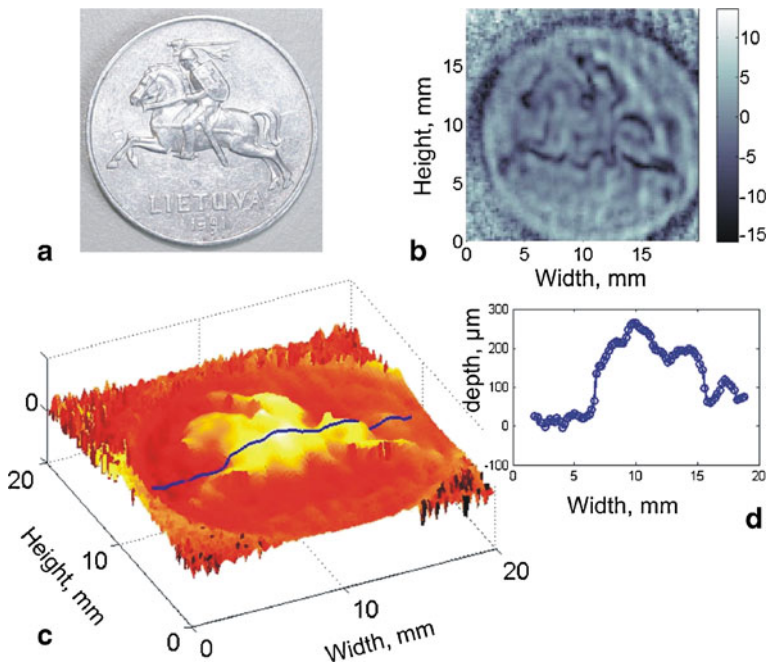


Fig. 7 Example for THz heterodyne imaging with a 150-nm-gate-length CMOS FET using plane-to-plane imaging in reflection geometry. **a** Photograph of a Lithuanian 2-cent coin; **b** THz power image of the coin with grey scale in dB; **c** phase information; **d** depth profile obtained from the measured phase image, track indicated in **c** by the blue line. Data reproduced from [48]

therefore appears to be attractive mainly in the form of subharmonic mixing, employing LO radiation at much lower frequency where power is available more abundantly. Here we performed initial tests with only at the fundamental frequency, by quasi-optical superposition of the image beam with an LO beam with a power of $247 \mu\text{W}$. In the image plane, each pixel received an average power of only 5 nW . However, for measurements at an effective frame rate of 12.5 Hz as before, the maximal dynamic range was measured to be 30 dB , 10 dB higher than in direct power detection mode. Figure 7 shows an example heterodyne image of a Lithuanian 2-cent coin acquired in reflection geometry.

This investigation showed that even a modest amount of LO power can improve the sensitivity by an appreciable degree. In addition, phase sensitivity becomes available which is useful for profilometry and depth reconstruction in three-dimensional imaging.

4 All-CMOS Imaging System

Finally, in Fig. 8a we present a raster-scan imaging system of which both emitter and detector have been fabricated in CMOS technology. The power is generated in a transmitter (TX) unit which was implemented in 90-nm CMOS technology [49].

This radiation source is the result of considerable developments addressing the challenge that emitters based on signal sources implemented in CMOS technology suffer in this frequency range from a low output power and a narrow frequency tuning range. For example, a 410-GHz 45-nm CMOS push-push voltage-controlled oscillator (VCO) provided a beam power of -47 dBm [10], a linear superposition technique implemented in 90-nm CMOS led to a power of -46 dBm at 324 GHz [50], and a 300-GHz fundamental VCO in 65-nm CMOS in [51] (power is not specified). However, new circuit design approaches for the regime around 200 GHz and beyond have been adopted in CMOS technologies and provide an improvement of

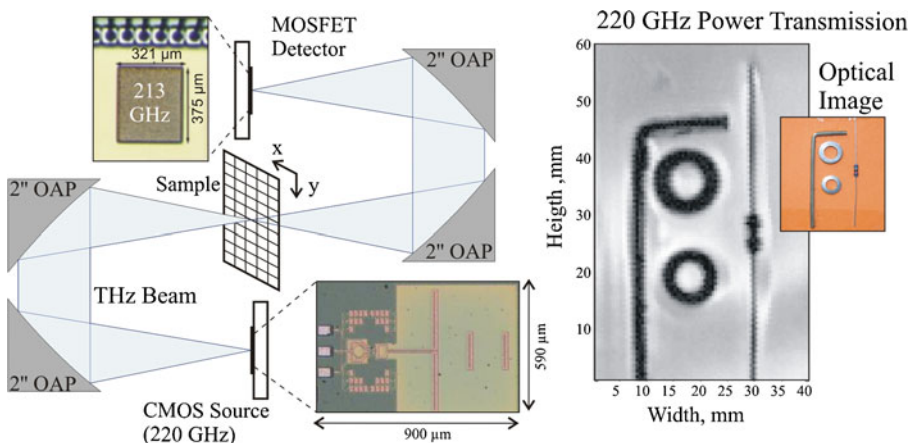


Fig. 8 **a** Full-CMOS imaging setup, **b** Recorded power transmission image of metallic targets

the output power which is sufficient to allow for practical applications. In particular, [52] reports an output power of -1.5 dBm which was achieved with a triple-push ring oscillator freely running at 288 GHz. The device was implemented in a 65-nm CMOS process and had integrated lens. Other examples, in brief: [53] reports a VCO made in 65-nm CMOS achieving a power of -9 dBm at 482 GHz; [54] describes a doubler realized in 65-nm CMOS generating -6.5 dBm at 244 GHz; [55] demonstrates a power of -7.2 dBm (radiated) at 280 GHz obtained with a 45-nm CMOS distributed active radiator (DAR) array. These sources suffer from narrow frequency tuning ranges. In contrast, the 90-nm CMOS TX device which we apply here and which is described in detail in [56], provides a rather wide tuning range from 210 to 227 GHz, and a maximal output power of -8.8 dBm at 217 GHz. The TX contains a differential Colpitts oscillator and an on-chip dipole antenna [49, 57]. The fundamental oscillation frequency of the VCO can be tuned in the 70–76 GHz frequency range. The working point of the active elements of the VCO is selected for efficient internal generation of the third-harmonic component which is guided to the antenna and emitted in the direction perpendicular to the chip plane.

A MOSFET detector (as those described earlier), designed for 213 GHz, was employed to detect the radiation and map out the radiation pattern. The considerably lower ratio between the patch height and wavelength resulted in the sensitivity of the detector at 213 GHz was 7 times lower than that of devices for 0.6 THz. The strongest emission was recorded for a 220 GHz frequency and the maximum output power of ~ 50 μ W assuming 6 dB power loss to the side lobes and limited collection aperture. The source was also characterized with an open-waveguide power detector as presented in [56]. There the peak emission is reported also at about 220 GHz with the estimated power of up to 135 μ W. Somewhat lower values obtained with imaging setup can be explained by its different sensitivity to the profile and direction of emitted radiation.

Imaging has been performed using a lock-in integration time constant of 50 ms and filter settings of 6 dB/oct which correspond to equivalent noise bandwidth of 5 Hz. The system SNR was measured to be 20 dB. Figure 8b demonstrates power transmission image of metallic targets. In this imaging system both sources and detectors can be easily combined into multi-element arrays. Therefore, it appears to be fairly straightforward to boost the performance by improving devices (a factor of 20 is possible on the detector side by improving detector design and radiation coupling) and the imaging set-up.

The results give us confidence that all-CMOS measurement and imaging systems for the range 200–300 GHz can be implemented in the near future. Furthermore, they encourage the integration of third-harmonic VCOs onto detector chips for the investigation of sub-harmonic mixing with on-chip-generated LO power in the near future, for coherent and highly sensitive detection with single or multiple pixels.

Higher frequencies can be accessed by using more advanced CMOS technology such as that used to 32-nm IBM SOI process used to implement a signal source at 240 GHz with significant performance [58]. By further optimization of the design to exploit higher harmonics as presented in [49], it appears realistic that a signals source can be implemented in the THz gap to pave the way for full imaging systems at THz frequencies based on all-CMOS devices.

The performance of the imaging system depends on the availability of a controllable, stable, and clean signal source. For this purpose, two approaches to be implemented in CMOS can be pursued and optimized for THz frequencies. The first one is injection locking of a tripler-based Coplitts VCO as introduced in [59], while the second one is an injection-locked frequency multiplier [60, 61]. Both approaches provide a wide frequency-locked tuning range and a high output power, and can be integrated in the near future onto the CMOS detector chips.

5 Summary

In summary we discuss on different modalities of THz setups exploiting silicon MOSFET detectors. It is expected that such devices will create a strong impact on further developments in THz photonics, and in particular for THz imaging, which can greatly profit from the strength of silicon technology the high fabrication yield, the uniformity and reliability of the devices, the low power consumption, and all in all—bringing the potential for strong cost reduction with increasing production rates.

Acknowledgments We are grateful to Alexander von Humboldt Foundation for funding the Institute Partnership between Vilnius and Frankfurt. German-Israeli Foundation for Scientific Research and Development is acknowledged for the grant no. 1173/2011. Frankfurt University acknowledges the grant Sensors Toward Terahertz within the LOEWE platform (1502-2995-11). A. Lisauskas is thankful to a Lithuanian Science Foundation for a grant VP1-3.1-SMM-07-K-03-040.

References

1. Handbook of Terahertz Technology for Imaging, Sensing and Communications, D. Saeedkia, Ed., Sawston, Cambridge, UK: Woodhead Publishing Ltd., 2013.
2. P. U. Jepsen, D. G. Cooke, and M. Koch, *Laser Photon. Rev.* 5, 124 (2011).
3. W. L. Chan, J. Deibel, and D. M. Mittleman, *Rep. Prog. Phys.* 70, 1325 (2007).
4. E. Pickwell and V. P. Wallace, *J. Phys. D: Appl. Phys.* 39, 301 (2006).
5. M. Nagel, P. Haring Bolivar, M. Brucherseifer, H. Kurz, A. Bosserhoff, and R. Büttner, *Appl. Opt.* 41, 2074 (2002).
6. N. Hasegawa, T. Löffler, M. Thomson, and H. G. Roskos, *Appl. Phys. Lett.* 83, 3996 (2003).
7. D. Banerjee, W. von Spiegel, M. D. Thomson, S. Schabel, and H. G. Roskos, *Opt. Express* 16, 9060 (2008).
8. K. B. Cooper, R. J. Dengler, N. Llombart, T. Bryllert, G. Chattopadhyay, E. Schlecht, J. Gill, C. Lee, A. Skalare, I. Mehdi, and P. H. Siegel, *IEEE Trans. Microwave Theory Techn.* 56, 2771 (2008).
9. F. Friederich, W. von Spiegel, M. Bauer, F. Z. Meng, M. D. Thomson, S. Boppel, A. Lisauskas, B. Hils, V. Krozer, A. Keil, T. Löffler, R. Henneberger, A. K. Huhn, G. Spickermann, P. Haring Bolivar, and H. G. Roskos, *IEEE THz Science Technol.* 1, 183 (2011).
10. E. Seok, D. Shim, C. Mao, R. Han, S. Sankaran, C. Cao, W. Knap, and K. K. O, *IEEE J. Solid-State Circ.* 45, 1554 (2010).
11. E. Öjefors, J. Grzyb, Y. Zhao, B. Heinemann, B. Tillack, and U. R. Pfeiffer, *Digest of the Solid-State Circuits Conference (ISSCC) 2011*, pp. 224–226 doi:[10.1109/ISSCC.2011.5746294](https://doi.org/10.1109/ISSCC.2011.5746294).
12. K. Statnikov, E. Öjefors, Y. Zhao, and U. R. Pfeiffer, *Proceeding of New Circuits and Systems Conference (NEWCAS) 2011*, pp. 261–264 doi:[10.1109/NEWCAS.2011.5981305](https://doi.org/10.1109/NEWCAS.2011.5981305).
13. S. Hu, Y.-Z. Xiong, B. Zhang, L. Wang, T.-G. Lim, M. Je, and M. Madihian, *IEEE J. Solid-State Circ.* 47, 2654 (2012).

14. W. Knap and D. I. Dyakonov, "Field effect transistors for terahertz applications", in: Handbook of Terahertz Technology for Imaging, Sensing, and Communications, D. Saeedkia, Ed., Sawston, Cambridge, UK: Woodhead Publishing Ltd., 2013, p. 121.
15. S. Boppel, A. Lisauskas, and H. G. Roskos, "Terahertz array imagers: towards the implementation of terahertz cameras with plasma-wave-based silicon MOSFET detectors", in: Handbook of Terahertz Technology for Imaging, Sensing, and Communications, D. Saeedkia, Ed., Sawston, Cambridge, UK: Woodhead Publishing Ltd., 2013, p. 231.
16. R. Al Hadi, H. Sherry, J. Grzyb, Y. Zhao, W. Forster, H. M. Keller, A. Cathelin, A. Kaiser, and U. R. Pfeiffer, *IEEE J. Solid-State Circ.* 47, 2999 (2012).
17. A. Lisauskas, S. Boppel, M. Saphar, V. Krozer, L. Minkevičius, D. Seliuta, I. Kašalynas, V. Tamošiūnas, G. Valušis, and H. G. Roskos, *Proc. SPIE* 8496, 8496–18 (2012).
18. R. Han, Y. Zhang, Y. Kim, D. Y. Kim, H. Shichijo, E. Afshari, and K. O, In Proceedings of ISSCC. 2012, 254–256.
19. J. Meilhan, F. Simoens, J. Lalanne-Dera, S. Gidon, G. Lasfargues, S. Pocas, D. T. Nguyen, J.-L. Ouvrier-Buffer, *Proc. of the 37th International Conference on Infrared, Millimeter and Terahertz Waves (IRMMW-THz)*, paper Thu-B-1-2 (2012).
20. N. Oda, *Comptes Rendus Physique* 11, 496 (2010).
21. M. Dyakonov and M. Shur, *IEEE Trans. Electron. Dev.* 43, 380 (1996).
22. A. Lisauskas, U. Pfeiffer, E. Öjefors, P. Haring Bolivar, D. Glaab, and H. G. Roskos, *J. Appl. Phys.* 105, 114511 (2009).
23. E. Öjefors, U. Pfeiffer, A. Lisauskas, and H. G. Roskos, *IEEE J. Solid-State Circ.* 44, 1968 (2009).
24. A. Lisauskas, D. Glaab, H. G. Roskos, E. Öjefors, and U. R. Pfeiffer, *Proc. SPIE* 7215, 72150J, (2009).
25. S. Boppel, A. Lisauskas, M. Mundt, D. Seliuta, L. Minkevičius, I. Kašalynas, G. Valušis, M. Mittendorff, S. Winnerl, V. Krozer, and H. G. Roskos, *IEEE Transactions on Microwave Theory and Techniques* 60, 3834 (2012).
26. S. Preu, S. Kim, R. Verma, P. G. Burke, M. S. Sherwin, and A. C. Gossard, *J. Appl. Phys.* 111, 024502 (2012).
27. W. Knap, V. Kachorovskii, Y. Deng, S. Rumyantsev, J.-Q. Lü, R. Gaska, M. S. Shur, G. Simin, X. Hu, M. Asif Khan, C. A. Saylor and L. C. Brunel, *J. Appl. Phys.* 91, 9346 (2002).
28. A. El Fatimy, F. Teppe, N. Dyakonova, W. Knap, D. Seliuta, G. Valušis, A. Shchepetov, Y. Roelens, S. Bollaert, A. Cappy, and S. Rumyantsev, *Appl. Phys. Lett.* 89, 131926 (2006).
29. W. Knap, H. Videlier, S. Nadar, D. Coquillat, N. Dyakonova, F. Teppe, M. Bialek, M. Grynberg, K. Karpierz, J. Lusakowski, K. Nogajewski, D. Seliuta, I. Kašalynas, and G. Valušis, *Opto-Electronics Rev.* 18, 225 (2010).
30. W. Knap, F. Teppe, Y. Meziani, N. Dyakonova, J. Lusakowski, F. Boeuf, T. Skotnicki, D. Maude, S. Rumyantsev, and M. S. Shur, *Appl. Phys. Lett.* 85, 675 (2004).
31. H. Sherry, R. Al Hadi, J. Grzyb, E. Öjefors, A. Cathelin, A. Kaiser, and U. R. Pfeiffer, *Proc. of the IEEE Radio Frequency Integrated Circuits Symposium (RFIC)*, 2011, doi:[10.1109/RFIC.2011.5940670](https://doi.org/10.1109/RFIC.2011.5940670).
32. S. Boppel, A. Lisauskas, V. Krozer, and H. G. Roskos, *Electron. Lett.* 47, 661 (2011).
33. F. Schuster, D. Coquillat, H. Videlier, M. Sakowicz, F. Teppe, L. Dussopt, B. Giffard, T. Skotnicki, and W. Knap, *Opt. Express* 19, 7827 (2011).
34. D. Veksler, F. Teppe, A. P. Dmitriev, V. Yu. Kachorovskii, W. Knap, and M. S. Shur, *Phys. Rev. B* 73, 125328 (2006).
35. T. A. Elkhatab, V. Yu. Kachorovskii, W. J. Stillman, S. Rumyantsev, X. C. Zhang, and M. S. Shur, *Appl. Phys. Lett.* 98, 243505 (2011).
36. F. Teppe, D. Veksler, V. Yu. Kachorovski, A. P. Dmitriev, X. Xie, X.-C. Zhang, S. Rumyantsev, W. Knap, and M. S. Shur, *Appl. Phys. Lett.* 87, 022102 (2005).
37. W. Stillman, C. Donais, S. Rumyantsev, M. Shur, D. Veksler, C. Hobbs, C. Smith, G. Bersuker, W. Taylor, and R. Jammy, *Int. J. High Speed Electron Syst.* 20, 27 (2011).
38. A. Lisauskas, S. Boppel, J. Matukas, V. Palenskis, L. Minkevičius, G. Valušis, P. Haring-Bolivar, and H. G. Roskos, *Appl. Phys. Lett.* 102, 153505 (2013).
39. B. Gershgorin, V. Kachorovskii, Y. Lvov, and M. Shur, *Electron. Lett.* 44, 1036 (2008).
40. D. Glaab, S. Boppel, A. Lisauskas, U. Pfeiffer, E. Öjefors, and H. G. Roskos, *Appl. Phys. Lett.* 96 (2010) 042106.
41. A. Lisauskas, S. Boppel, M. Mundt, V. Krozer, and H. G. Roskos, *IEEE Sensors J.* 13, 124 (2013).

42. S. Boppel, M. Mundt, A. Lisauskas, and H. G. Roskos, "Direct, heterodyne, and subharmonic CMOS FET-based THz detection: From device modeling to rational design and evaluation", in "High-speed devices and circuits with THz applications", J. Choi and K. Iniewski, Eds., Springer, to be published.
43. T. Trzcinski, N. Palka, and M. Szustakowski, *Bulletin of the Polish Academy of Sciences: Technical Sciences* 59, 445 (2011).
44. I. Kašalynas, R. Venckevičius, D. Seliuta, I. Grigelionis, and G. Valušis, *J. Appl. Phys.* 110, 114505 (2011).
45. M. Bolduc, M. Terroux, B. Tremblay, L. Marchese, E. Savard, M. Doucet, H. Oulachgar, C. Alain, H. Jerominek, and A. Bergeron, *Proc. SPIE* 8023, 80230C (2011).
46. J. Oden, J. Meilhan, J. Lalanne-Dera, J.-F. Roux, F. Garet, J.-L. Coutaz, and F. Simoens, *Optics Express* 21, 4817 (2013).
47. S. Boppel, A. Lisauskas, A. Max, V. Krozer, and H. G. Roskos, *Opt. Lett.* 37, 536 (2012).
48. S. Boppel, A. Lisauskas, M. Saphar, V. Krozer, and H. G. Roskos, in *Proc. 19th Microwave Radar and Wireless Communications Conference* (2012) doi:[10.1109/MIKON.2012.6233510](https://doi.org/10.1109/MIKON.2012.6233510).
49. B. Khamaisi and E. Socher, *IEEE Microw. Wireless Compon. Lett.* 22, 260 (2012).
50. Huang, D., et al., *IEEE J. Solid-State Circ.* 43, 2730 (2008).
51. Razavi, B., *IEEE J. Solid-State Circ.* 46, 894 (2011).
52. Y. Zhao, J. Grzyb, and U. R. Pfeiffer, in *Eur. Solid-State Circuits Conf. (ESSCIRC)*, p. 289 (2012) doi:[10.1109/ESSCIRC.2012.6341311](https://doi.org/10.1109/ESSCIRC.2012.6341311).
53. O. Momeni and E. Afshari, *IEEE J. Solid-State Circ.*, 46, 583 (2011).
54. O. Momeni and E. Afshari, *IEEE J. Solid-State Circ.* 46, 2966 (2011).
55. K. Sengupta and A. Hajimiri, in *Proceedings Int. Solid-State Circuits Conf. (ISSCC)* 2012, 256.
56. B. Khamaisi, S. Jameson and E. Socher, *IEEE Trans. Terahertz Science Technol.* 3, 141 (2013).
57. E. Socher and S. Jameson, *Electron. Lett.* 47, 1227 (2011).
58. N. Landsberg and E. Socher, accepted to *IEEE International Microwave Symposium (IMS)* 2013.
59. A. Vishnipolsky and E. Socher, *IEEE Topical Meeting on Silicon Monolithic Integrated Circuits in RF Systems (SiRF)* 2012, p. 136.
60. N. Mazor and E. Socher, *IEEE Microw. Wireless Comp. Lett.* 22, 424 (2012).
61. N. Mazor and E. Socher, *IEEE Trans. Microw. Theory Techn.* 61, 1924 (2013).